

# Spatio-temporally Varying Manning Roughness in Rivers and Streams: A calibration approach using in-situ water level and UAS altimetry

Jun Liu (✉ [juli@env.dtu.dk](mailto:juli@env.dtu.dk))

Department of Environmental Engineering, Technical University of Denmark

Liguang Jiang

School of Environmental Science and Engineering, Southern University of Science and Technology,

Filippo Bandini

Department of Environmental Engineering, Technical University of Denmark

Cécile Marie Margaretha Kittel

DHI-GRAS

Nicola Balbarini

DHI A/S

Nisha Gill Hansted

DHI A/S

Henrik Grosen

Dronesystems

Peter Bauer-Gottwein

Department of Environmental Engineering, Technical University of Denmark

---

## Research Article

**Keywords:** Manning roughness, steady-state solver, hydrodynamic modeling, UAS altimetry, global optimization

**Posted Date:** December 3rd, 2021

**DOI:** <https://doi.org/10.21203/rs.3.rs-1107960/v1>

**License:** © ⓘ This work is licensed under a Creative Commons Attribution 4.0 International License.

[Read Full License](#)

---

# 1 Spatio-temporally Varying Manning Roughness in Rivers and Streams: A 2 calibration approach using in-situ water level and UAS altimetry

3 Jun Liu<sup>1</sup>, Liguang Jiang<sup>2</sup>, Filippo Bandini<sup>1</sup>, Cecile M. M. Kittel<sup>3</sup>, Nicola Balbarini<sup>4</sup>, Nisha G.  
4 Hansted<sup>4</sup>, Henrik Grosen<sup>5</sup>, Peter Bauer-Gottwein<sup>1</sup>

5 <sup>1</sup>Department of Environmental Engineering, Technical University of Denmark, Kgs. Lyngby, 2800, Denmark

6 <sup>2</sup>School of Environmental Science and Engineering, Southern University of Science and Technology,  
7 Shenzhen, China

8 <sup>3</sup>DHI-GRAS, Hørsholm, 2970, Denmark

9 <sup>4</sup>DHI A/S, Agern Allé 5, 2970 Hørsholm, Denmark

10 <sup>5</sup>Dronesystems, Finlandsgade 25F, Denmark

## 11 **Abstract**

12 Hydraulic roughness (expressed in terms of e.g. Manning's roughness coefficient) is an important input to hydraulic  
13 and hydrodynamic simulation models. One way to estimate roughness parameters is by hydraulic inversion, using  
14 observed water surface elevation (WSE) collected from gauging stations, satellite platforms or UAS (Unmanned  
15 Aerial System) -based altimeters. Specifically, UAS altimetry provides close to instantaneous observations of  
16 longitudinal profiles and seasonal variations of WSE for various river types, which are useful for calibrating  
17 roughness parameters. However, it is computationally expensive to run high-resolution hydrodynamic models for  
18 long simulation periods (e.g. multiple years), and thus global optimization of spatially and temporally distributed  
19 parameter sets for such models, e.g., spatio-temporally varying river roughness, is still challenging.

20 This study presented an efficient calibration approach for hydraulic models, using a simplified steady-state  
21 hydraulic solver, UAS altimetry datasets, and in-situ observations. The calibration approach minimized the  
22 weighted sum of a misfit term, spatial smoothness penalty, and a sinusoidal a priori temporal variation constraint.  
23 The approach was first demonstrated for several synthetic calibration experiments and the results indicated that  
24 the global search algorithm accurately recovered the Manning–Strickler coefficients  $M$  for short river reaches  
25 in different seasons, and  $M$  varied significantly in time (due to the seasonal growth cycle of the aquatic  
26 vegetation) and space (due to, e.g. spatially variable vegetation density). Subsequently, the calibration approach  
27 was demonstrated for a real WSE dataset collected at a Danish test site, i.e., Vejle Å. Results indicated that  
28 spatio-temporal variation in  $M$  was required to accurately fit in-situ and UAS altimetry WSE observations. This  
29 study illustrated how UAS altimetry and hydraulic modeling can be combined to achieve improved  
30 understanding and better parameterization of small and medium-sized rivers, where conveyance is controlled  
31 by vegetation growth and other spatio-temporally variable factors.

32 **Key Words:** Manning roughness, steady-state solver, hydrodynamic modeling, UAS altimetry, global  
33 optimization.

34

## 35 **1. Introduction**

36 Improving the management of floods and significantly reducing their influence on public health,  
37 economic activities, and the environment is one of the Sustainable Development Goals (Lee et al., 2020).  
38 Climate variability and change and the increased pressure from anthropogenic activities have impacted the  
39 frequency and severity of floods on regional and global scales, which are extremely difficult to predict  
40 accurately (Blöschl et al., 2020; Knox, 1993; Sauer et al., 2021). Hydrodynamic/hydraulic models are valuable  
41 tools to estimate variations of flows and water levels along river courses; widely used modeling tools include  
42 MIKE Hydro River, LISFLOOD, and HEC-RAS, which are purposeful for developing flood simulation and  
43 early-warning systems (Rokaya et al., 2020; Shi et al., 2015). However, it is computationally expensive to run  
44 these models on a seasonal time scale, and to estimate spatiotemporally variable parameter fields because of  
45 high computational load, large numbers of unknown parameters, and input data requirements (Hunter et al.,  
46 2007).

47 Empirical estimation and calibration of unobserved parameters, such as river roughness and bed  
48 geometry (which may only be available for a few points along the river), is a central task in the development of  
49 real-world hydraulic and hydrodynamic models. River roughness is an effective parameter representing friction  
50 effects in the shallow water equations. It is a critical controlling parameter for conveyance estimation and thus  
51 water levels in rivers and streams. The parameter is influenced by many factors, such as the type of the bed and  
52 bank materials, aquatic vegetation, surface irregularity, shape and size of the channel cross-section, the  
53 meandering character of the river channel, and state of flow motion (Cowan, 1956). Some studies have  
54 emphasized the identification of spatially distributed roughness parameters (Attari et al., 2021; Attari and  
55 Hosseini, 2019; Jiang et al., 2020; Mtamba et al., 2015; Werner et al., 2005; Ye et al., 2018). Li et al. (1992)  
56 developed a predictive model for mean flow in irregular natural rivers, and the results indicated that the effective  
57 resistance was strongly influenced by river cross-sectional nonuniformity, and the authors pointed out that  
58 sampling density for geometric parameters should depend on the degree of stream irregularity. Tuozzolo et al.  
59 (2019) further analyzed the impact of reach averaging Manning's equation and showed that roughness varied  
60 significantly even in a 6.5 km river stretch.

61 Meanwhile, seasonal variations in discharge and aquatic vegetation (type, height, and density) also  
62 profoundly impact the flow resistance, especially for many lowland vegetated river channels (Marjoribanks et  
63 al., 2014). The seasonal growth of aquatic macrophytes can significantly increase bed resistance, which leads  
64 to a decrease of river channel conveyance and consequently may increase flood risk. Aquatic vegetation in rivers  
65 is therefore regularly monitored and managed in some regions, such as Denmark. Jiang et al. (2020) found that

66 the Gauckler–Strickler coefficient  $K_s$  ( $K_s = 1/n$ ) increased significantly after vegetation was cut. However,  
67 simultaneously calibrating roughness parameters in both spatial and temporal scales is seldom reported.

68 The calibration of spatiotemporally varying river roughness requires dense sampling of the water  
69 surface elevation (WSE) in both time and space. Gauging stations and satellite altimetry are two widely used  
70 methods to retrieve WSE observations. Gauged WSE is only available at discretely distributed points in space,  
71 although the measurements are approximately continuous in time. Satellite altimeters, especially geodetic  
72 missions, such as CryoSat-2, have high spatial resolution but low temporal resolution and generally deliver high  
73 data quality only over large rivers (minimum width ca. 100 m). Considering the limitations of space-borne  
74 missions in monitoring small rivers, Unmanned Aerial Systems (UAS) have also been used for fluvial  
75 environments monitoring in recent years. The advantages of UAS for river systems monitoring comprise  
76 retrieval of data with a very high spatial resolution and accuracy, surveying inaccessible or cost-prohibitive  
77 areas, low-altitude flight, low-cost and flexible payload design (Vélez-Nicolás et al., 2021). Bandini et al. (2020)  
78 developed a radar altimetry system onboard lightweight UAS, measuring the range between sensors and water  
79 surface. WSE was calculated by subtracting the range from sensor height, retrieved by the GNSS receiver. The  
80 radar altimetry system was further applied in small vegetated streams (1-2 m wide), and the accuracy of WSE  
81 measurements outperformed LiDAR and photogrammetry methods by one order of magnitude (Bandini et al.,  
82 2020). WSE measurements from UAS radar altimetry, were further used for spatial river roughness calibration  
83 by Jiang et al. (2020).

84 Automatic calibration of unobserved or unobservable parameters proceeds by changing model  
85 parameters until the value of simulated variables matches the observed truth or the residual drops into an  
86 acceptable range, presuming that the resulting parameters are optimal values. Previous hydraulic inversion  
87 studies mainly used local search algorithms such as Levenberg-Marquardt (Jiang et al., 2020, 2019), for  
88 calibrating parameters of hydrodynamic models due to the high computational cost of the forward simulation  
89 models. However, such algorithms cannot guarantee a global optimum and may perform poorly in highly  
90 parameterized and non-linear inverse problems. Global optimization methods are more suitable and have a high  
91 probability of successfully finding the optimal parameter set (Duan et al., 1992, 1993). Still, global search  
92 algorithms require more runs of the forward simulation model (Kittel et al., 2021).

93 This study proposed the estimation of optimal spatiotemporally varying Manning–Strickler coefficients  
94 using station data and UAS altimetry. Considering station data characterized by high-temporal resolution (daily  
95 or sub-daily) but coarse and discrete distribution in space, and UAS altimetry with high-spatial resolution and  
96 accuracy (centimeter level) but sporadic coverage in time, the present study explored the value of  
97 simultaneously using both in-situ and UAS observations of WSE for Manning–Strickler coefficients calibration.  
98 The methodology was first evaluated using different synthetic calibration experiments, considering data  
99 availability and uncertainty in a medium-sized stream. Subsequently, high spatial-temporally distributed

100 roughness parameters for the stream was calibrated and validated using real-world WSE data collected from  
101 gauging stations and UAS.

102

## 103 2. Materials and methods

### 104 2.1. Calibration approach

105 Forward simulation models, observations, and search algorithms are critical elements for calibrating  
106 unknown parameters in hydraulic and hydrodynamic models. In this study, we aimed to calibrate  
107 spatiotemporally variable roughness parameters, which involved hundreds of individual parameter values. A  
108 simplified hydraulic model, a global search algorithm and appropriate regularization terms were used to  
109 guarantee an efficient and effective parameter estimation.

110 We assumed that the effective roughness in each small river stretch  $x$  was constant, and the roughness  
111 parameters were also stable over a short time interval  $t$ , e.g., a month in this study. Thus, we had a  
112 spatiotemporally varying-parameter  $M(x, t)$ , the symbol  $M$  is the Manning–Strickler coefficient;  $M = 1/n$ ,  $n$   
113 being Manning's roughness coefficient. Considering that a large number of parameters needs to be calibrated,  
114 the objective function for the optimization algorithm should be regularized. Here, the objective function  
115 comprised a *misfit* term and two *regularization* terms. The *misfit* term was set to measure the weighted  
116 squared difference between the simulated WSE and the observed truth. The *regularization* terms were used  
117 to constrain the variations of the parameters. The objective function ( $\emptyset$ ) was presented as:

$$118 \quad \emptyset = w \cdot \text{misfit} + (1 - w) \cdot \text{regularization} \quad (1)$$

119 Where  $w$  was the weight between *misfit*, and *regularization*.

120 The misfit is the difference between the model simulations ( $WSE_{sim}$ ) and the observations ( $WSE_{obs}$ )  
121 at all the time steps ( $N_t$ ) and chainage points ( $N_x$ ). The observations included in-situ WSE and UAS altimetry,  
122 with different uncertainties ( $\sigma_m$ ). The misfit was calculated by the following equation:

$$123 \quad \text{misfit} = \sum_{t=1}^{N_t} \sum_{x=1}^{N_x} \left( \frac{WSE_{sim}(x, t) - WSE_{obs}(x, t)}{\sigma_m} \right)^2 \quad (2)$$

124 Regularization terms included a spatial smoothness and an a priori sinusoidal:

$$125 \quad \text{regularization} = \lambda \cdot \text{smoothness} + (1 - \lambda) \cdot \text{apriori}$$

126 Where  $\lambda$  is the weight between smoothness and a priori term.

127 The smoothness term was based on the fact that the river channel conditions (e.g., size and type of the  
128 bed and bank materials, shape of the cross section, and longitudinal variation in cross-sectional shapes) change

129 continuously in space and the roughness parameters along the river channel was expected to change smoothly.  
130 The smoothness term was expressed using a standard first-order roughening term, i.e.

$$131 \quad \text{Smoothness} = \sum_{x=1}^{Nx} \left( \frac{M(x) - M_{neighbor}(x-1)}{\sigma_{smooth}} \right)^2 \quad (3)$$

132 Where the  $\sigma_{smooth}$  is a typical variation between neighbors in space.

133 Considering that the inter-annual and seasonal variations of the discharge and vegetation growth periods,  
134 we assumed that the temporal variations of river roughness have a sinusoidal regular pattern. For example, the  
135 Manning–Strickler coefficient in Danish rivers has a large seasonal variation with the minimum value in the  
136 summer season and maximum value in the winter season. Thus, we assumed an a priori sinusoidal seasonal  
137 variation of M:

$$138 \quad M_{apriori}(x, t) = M_0(x) + A_0(x) \sin(\omega t + \varphi) \quad (4)$$

139 The parameters in the sinusoidal equation are unknown and are estimated by regression for each candidate  
140 parameter set. A corresponding a-priori constraint is introduced in the objective function to stabilize temporal  
141 variations of the estimated parameters:

$$142 \quad \text{Apriori} = \sum_{t=1}^{Nt} \left( \frac{M(x, t) - M_{apriori}(x, t)}{\sigma_{apriori}} \right)^2 \quad (5)$$

143 Where  $\sigma_{apriori}$  is a typical deviation from the a priori sinusoidal seasonal model.

## 144 2.2. Optimization algorithms

145 A global search algorithm, the Shuffled Complex Evolution algorithm of the University of Arizona  
146 (SCE-UA), was used to calibrate the Manning–Strickler coefficients M in the present study. The algorithm has  
147 been widely used for different search problems. It includes features such as the combination of random and  
148 deterministic approaches, an implicit clustering strategy, and a systematic complex evolution strategy. More  
149 detail about this optimization method can be found in Duan et al. (1992, 1993). SCE-UA has been integrated  
150 into the open-source python package, Statistical Parameter Optimization Tool (Houska et al., 2015). To  
151 determine how many iterations are required to get reliable information about the bulk of parameters, the number  
152 of iterations is calculated by the methods provided by Henkel et al. (2012).

## 153 2.3. Forward simulation model

### 154 2.3.1. Steady-state hydraulic solver

155 An efficient forward simulation model is critical for the global optimization. Though the shallow-water  
156 equations are simplified one-dimensional forward model, solutions at seasonal time scales are still time  
157 consuming. Considering the number of parameters and the required repetitions of the forward solver in the

158 present study, improvements of the efficiency of the forward simulation model will greatly save calibration time.  
159 Thus, an efficient steady-state hydraulic solver was used.

160 The simplified hydraulic solver is based on the Saint-Venant equations, assuming that the water flow  
161 is in the condition of steady-state, i.e., all quantities are invariable in time. The development of the solver is  
162 described fully in Kittel et al. (2021). Only the main formulas of the solver therefore are presented here.

163 The momentum balance equation under steady-state is presented as:

$$164 \quad \frac{\partial}{\partial x} \left( \frac{Q^2}{A} \right) + gA \frac{dh}{dx} - gA(S_0 - S_f) = 0 \quad (8)$$

165 Where A is flow cross-sectional area, Q is volumetric discharge, x is the chainage, g is the gravitational  
166 constant, h is flow depth,  $S_0$  is the bed slope,  $S_f$  is the friction slope. The general form of the equation was  
167 organized by taking the partial derivative of the area relative to the chainage and width, and isolating the change  
168 in depth over the chainage:

$$169 \quad \frac{dh}{dx} = \frac{\left( \frac{Q^2}{gA^3} \frac{\partial A}{\partial x} + S_0 - S_f + \frac{2Q \times q}{gA^2} \right)}{\left( 1 - \frac{Q^2}{gA^3} \frac{\partial A}{\partial h} \right)} \quad (9)$$

170 Where  $S_0$  is calculated using river bed elevation (z) and chainage as (  $-dz/dx$ ),  $S_f$  is the river channel  
171 friction and can be calculated using Manning's equation:

$$172 \quad Q = MAR^{\frac{2}{3}} S_f^{\frac{1}{2}} \quad (10)$$

173 R is the hydraulic radius. Equation (9) was solved explicitly. We used a grid spacing of  $\Delta x = 20$  m, and  
174 the hydraulic parameters, i.e., area, depth, bed elevation, were interpolated for each calculation grid point from  
175 neighboring cross sections.

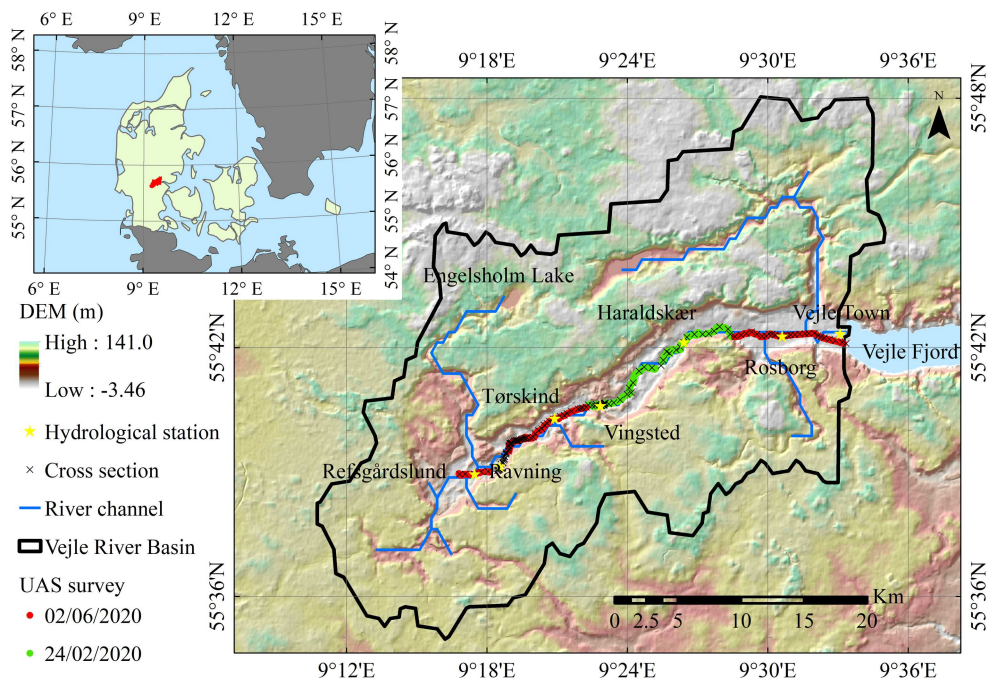
### 176 2.3.2. MIKE HYDRO River

177 MIKE Hydro River was used to create synthetic WSE observations and validate the calibrated spatio-  
178 temporal Manning–Strickler coefficients M. MIKE HYDRO River is a one-dimensional (1D) computational  
179 engine for modeling fully unsteady flows in river networks, pipe networks, and estuaries. The modeling system  
180 is dependent on an implicit, finite difference numerical solution of the shallow water equations, which are  
181 transformed into a set of implicit finite difference equations on a computational staggered grid consisting of  
182 alternating q- and h-grid points, i.e. points where the discharge, q, and water level h, respectively. The  
183 computational grid is generated automatically based on the user requirements, but the lower value of the grid  
184 spacing needs more calculations.

### 185 2.4. Case study site

186 Vejle Å (Vejle River) is a natural stream located in Vejle Municipality, Denmark, which is a typical  
 187 lowland river with mild slopes and meandering character. It originates from Engelsholm Sø and empties into  
 188 Vejle Fjord, with an approximate length of 36.7 km (Fig. 1). The stream flows through woods, farmland, bush,  
 189 grassland, and urban regions, with the riverbank densely covered with shrubs, trees, and weeds. The dense  
 190 vegetation in the Vejle Å increases friction in the river channel and raises the water level. It is necessary to cut  
 191 the submerged vegetation in the river during the flooding season to improve river channel conveyance.

192 Some downstream areas, e.g., Haraldskær, Vejle city, have been plagued by flooding almost every year,  
 193 following cloudbursts, extreme precipitation events, and storm surges. Thus, river management and flood  
 194 prediction are vital in this area. The calibration approach was tested in the 23.90 km long river reach between  
 195 Refsgårdslund and Vejle Harbor. Seven hydrological stations are located in this reach. Water level and discharge  
 196 data were available every 15 minutes, and rating curves interpolated the corresponding discharge data.



197  
 198 Figure 1. Field site and channel views. The upper left map showing the study area (Vejle river basin colored in  
 199 red) in the southeastern part of Jutland, Denmark. The lower right figure shows the studied reach of Vejle Å,  
 200 including river channel, cross section, in-situ stations and UAS routes.

201 2.5. In-situ data availability

202 2.5.1. Discharge

203 Discharge data were obtained from two hydrological stations, Refsgårdslund and Haraldskær, in the  
 204 period of 01/08/2018 and 26/08/2020. Fig. A1 shows the flow regime of the Vejle River. The discharge is  
 205 unevenly distributed during the year, and the discharge is low in the warm season and high in the cold season.  
 206 The annual average discharge in Refsgårdslund and Haraldskær were 3.03 m<sup>3</sup>/s and 4.19 m<sup>3</sup>/s, respectively. The

207 maximum daily discharge during the period is 10.68 m<sup>3</sup>/s and 16.13 m<sup>3</sup>/s. There are no influential tributaries in  
208 the chainage interval between Refsgårdslund and Haraldskær, and, therefore, we assumed that the lateral inflow  
209 is uniformly distributed between stations Refsgårdslund and Haraldskær.

#### 210 2.5.2. Water surface elevation

211 Water surface elevation data was collected from five hydrological stations, i.e., Tørskind (14.77 km),  
212 Ravning (18.92 km), Vingsted (21.29 km), Rosborg (33.56 km), and Vejle Havn (36.57 km), and the data are  
213 displayed in Fig. A2. The time resolution of the WSE data is 15 minutes. The river surface has an average slope  
214 of 5.8 ‰ between upstream Refsgårdslund and the outlet to the sea. WSE of Vejle Havn was used as the  
215 downstream boundary of the hydraulic and hydrodynamic models while the other stations were used for  
216 calibration.

#### 217 2.5.3. Cross sections

218 The cross-section information was obtained from the national information system run by WSP Denmark,  
219 and 130 cross-sections were included from Refsgårdslund to Vejle harbor. The raw cross-section data includes  
220 the distance from the left levee and the corresponding depth. The raw data were then put into MIKE Zero  
221 software for further processing. The processed cross-sections contain hydraulic parameters including width,  
222 hydraulic radius, bed elevation, submerged cross-sectional area, and the depth at a specific WSE. The basic  
223 information of all bank-full cross-sections is shown in appendix (Fig. A3). The river channel is narrow and deep  
224 in the upstream area, wide and shallow in the downstream area. The bank-full submerged area does not increase  
225 from upstream to downstream, which is a likely cause of increased flood risk, e.g., the cross-sectional area near  
226 Haraldskær located at chainage of 28.13 km is reduced and this area suffered from frequent floods. The river  
227 has a width of up to 20.84 m for bank-full depth in Refsgårdslund to 49.87 m in Vejle Havn. The maximum  
228 depth is 4.36 m in the upstream and 2.34 m in Vejle Havn.

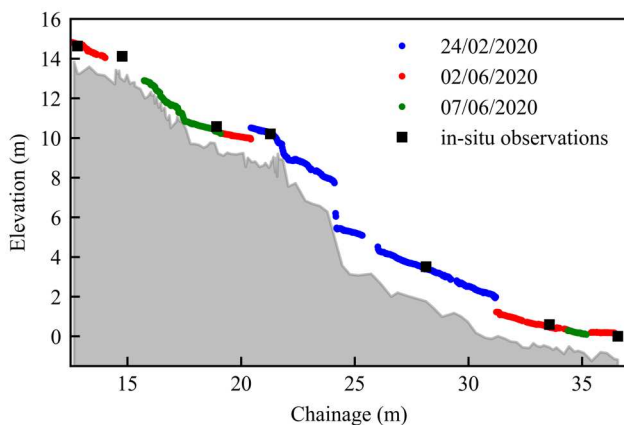
#### 229 2.6. UAS altimetry data collection and processing

230 The UAS-borne WSE measurement system used in this study was developed by Bandini et al. (2020).  
231 This system can measure accurate and distributed high-resolution WSE for small-size and vegetation-covered  
232 streams. The system uses a lightweight hexacopter drone equipped with a dual-frequency differential Global  
233 Navigation Satellite System (GNSS) and a 77 GHz radar chip with full waveform analysis to measure WSE  
234 (Bandini et al., 2020).

235 Several field campaigns were implemented from 2018 to 2020 by DTU Environment and Drone  
236 Systems (<https://dronesystems.dk>). Two long-distance UAS surveys were carried out in February and June 2020,  
237 which covered a river reach with a total length over 20 km (Fig. 2). The weather conditions and power supply  
238 infrastructure are the main constraining factors for the drone survey, and a one-kilometer-long river stretch can  
239 be measured in approximately 15 minutes. UAS altimetry data processing included post-processed kinematic  
240 (PPK) processing of the drone position, full-waveform analysis of the radar returns and data filtering. The

241 processed data was further filtered by a river mask to guarantee that the radar observations were captured above  
242 river water surface. The water mask was generated by buffering the river center line by 5 meters in each side.  
243 Detailed information of the UAS radar altimetry post-processing can be found in Bandini et al. (2020).

244 UAS altimetry shows great potential in delivering high-resolution WSE observations, as illustrated in  
245 Fig. 2. The water surface slope is clearly shown, which would not be obtainable from discrete gauging stations.  
246 UAS altimetry WSE matches in-situ measurement very well with mean square error lower than 0.03 m. There  
247 was no significant difference of data accuracy between the different surveys, although some deviations occurred  
248 between UAS altimetry and nearby in-situ stations.

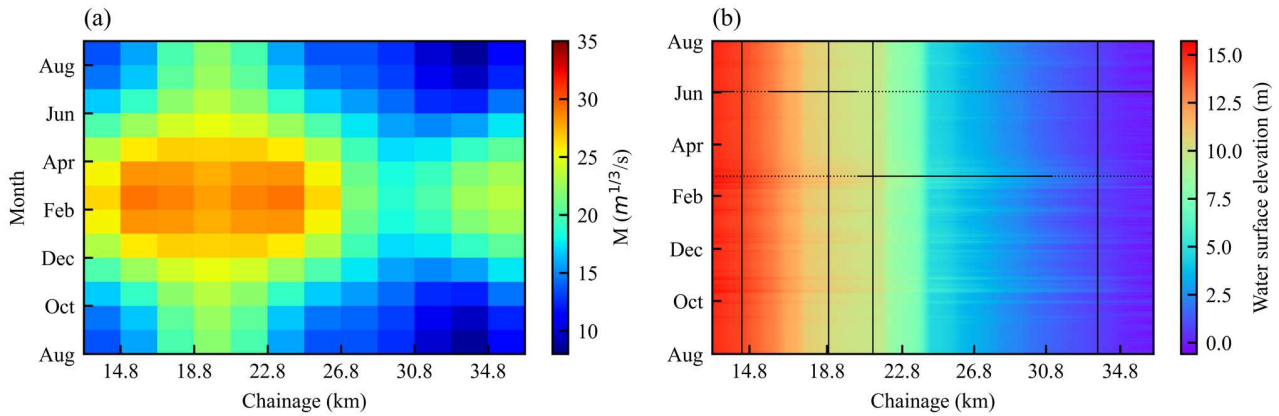


249

250 Figure 2. Longitudinal profile plots of WSE derived from UAS campaigns and in-situ measurements. The  
251 shaded area indicates the channel bed, which is represented by the deepest point in each cross-section.

## 252 2.7. Synthetic calibration experiments

253 The objective of synthetic studies is to conduct experiments in a controlled environment and allow the  
254 results to be compared with a synthetic truth. The synthetic truth for WSE was created by running the MIKE  
255 HYDRO River in fully dynamic mode to approximate the real situation. The standard boundary conditions for  
256 MIKE HYDRO River include upstream discharge from Refsgårdslund, lateral inflow interpolated between  
257 Refsgårdslund and Haraldskær, as well as downstream WSE from Vejle harbor. The overall control settings for  
258 model simulations were first initialized, including the simulation period was 2019-8-1 to 2020-8-1, time step  
259 length was one minute, computational grid spacing was 20 m, the branch started from chainage 12.8 km to 36.6  
260 km, raw data of 130 cross-sections, and the simulated results have a storing frequency of one day. The synthetic  
261 Manning–Strickler coefficients  $M$  is created with seasonal sinusoidal variation (Fig. 3).



262

263 Figure 3. Synthetic truth creation, including the (a) synthetic Manning–Strickler coefficients ( $M$ ), and (b) the  
 264 synthetic truth for water surface elevation with the vertical lines showing the temporal WSE data and the  
 265 horizontal lines showing the spatial UAS altimetry fully (in dash) and partially (in solid) covered the stretch of  
 266 river.

267 Several synthetic calibration scenarios were created to verify the value of UAS altimetry and in-situ  
 268 observations for varying  $M$  calibration under different situations of data availability. In the description of each  
 269 scenario for synthetic studies, the UAS altimetry referred to the longitudinal profiles of WSE (horizontal lines  
 270 in Figure 3b). In-situ data referred to the time series of water level (vertical lines in Figure 3b). The settings for  
 271 the three scenarios are as follows:

272 Scenario 1: Calibration of spatially varying  $M$  using UAS altimetry on different days. This scenario  
 273 corresponded to the situations when we collected UAS altimetry covering a long river stretch on a particular  
 274 day, e.g., February 24, 2020, and June 02, 2020. We want to answer two questions in this scenario: ( i ) whether  
 275 UAS altimetry with full and partial coverage can be successfully used for spatially distributed  $M$  calibration;  
 276 ( ii ) how the uncertainty of UAS altimetry affects the calibration. Although the real-world drone survey in June  
 277 was carried out over two different days, we assumed instantaneous data collection on a single day in the  
 278 synthetic experiment. 02/24/2020, and 06/02/2020 with full and partial coverage of UAS altimetry were selected  
 279 to conduct the calibration. Three different sets of noise (1 cm, 3 cm, and 10 cm) are assigned to the synthetic  
 280 truth of WSE. The steady-state hydraulic solver and SCE-UA global optimization were used to calibrate  $M$  for  
 281 each day separately and thus, no a-priori constraint on the temporal variation was applied.

282 Scenario 2: Calibration of spatiotemporally varying  $M$  using adequate UAS altimetry; this scenario  
 283 ideally assumed that UAS altimetry datasets were available on multiple days, evenly distributed in time.  
 284 Additionally, the UAS altimetry was collected on days when flow in the river are approximately steady-state.  
 285 We selected additional suitable steady-state days, approximately evenly distributed throughout the period of  
 286 interest (1-2 days per month or so). The varying Gauckler-Strickler coefficient, i.e.,  $M(x, t)$ , was calibrated using  
 287 the steady-state model as forward simulator and the global optimization as the searching engine.

288 Scenario 3: Calibration of spatiotemporally varying  $M$  utilizing a selection of in-situ data and UAS  
289 altimetry. This scenario approximated reality when we only have UAS altimetry for limited days and discretely  
290 distributed station data. Besides, the UAS altimetry does only partially cover the reach of interest, as shown in  
291 Figure 3. Because of the computational constraints, we still selected one day per month. Among the chosen  
292 dates, two dates were covered by partial UAS altimetry, i.e., 02/24/2020 and 06/02/2020, and the remaining  
293 dates only have WSE from 4 stations. UAS altimetry has a dense sampling compared to the in-situ data, and an  
294 appropriate weight must be chosen to balance the contributions of UAS and in-situ datasets to the total misfit  
295 term. The steady-state solver and global optimization were used for  $M$  calibration in this scenario.

296 Scenario 4: Real-world calibration of the spatiotemporally varying  $M$ . The configuration of the Steady-  
297 State solver and objective functions were the same as Scenario 3 but with the real WSE from in-situ observations  
298 and UAS altimetry.

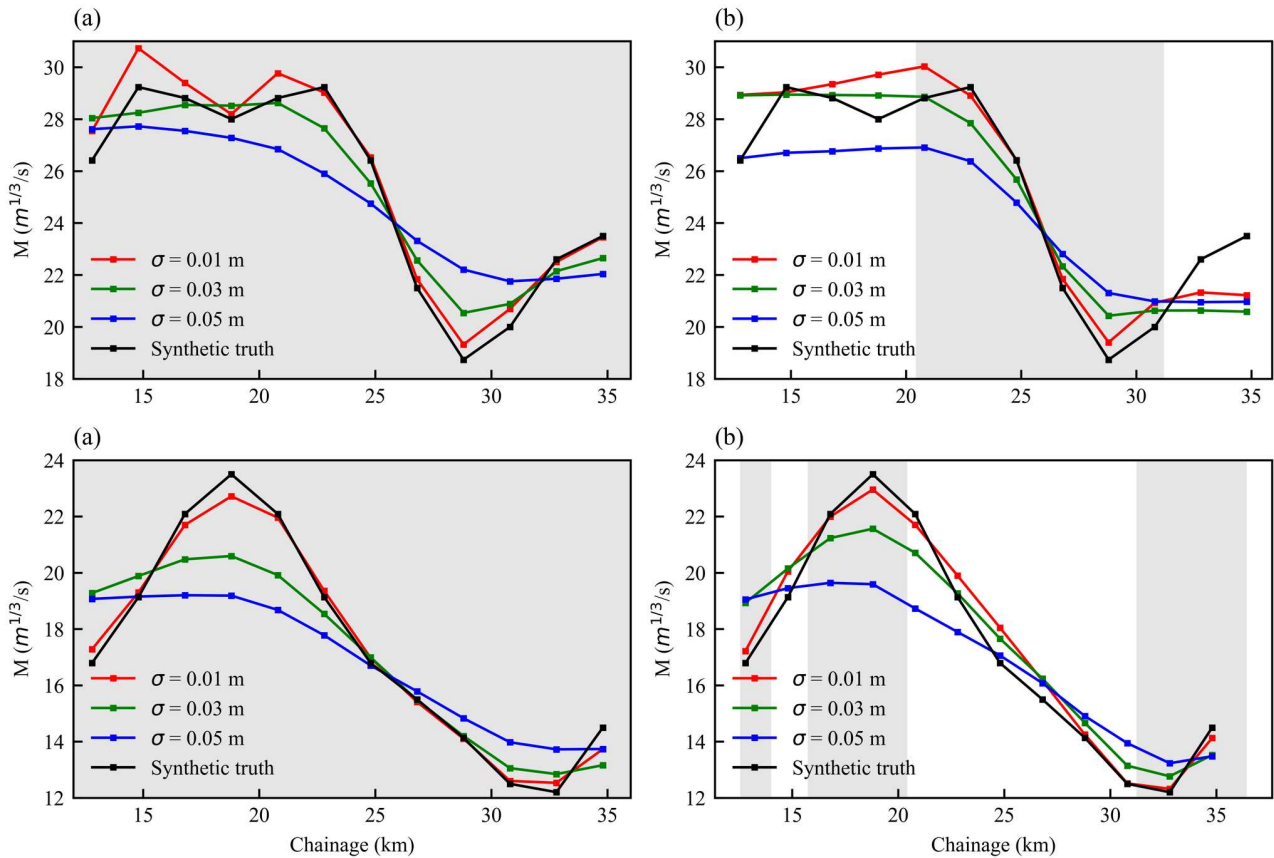
### 299 3. Results

#### 300 3.1. Synthetic experiment

301 The calibrated Manning–Strickler coefficients  $M$  in Scenario 1 approximated the synthetic truth, as  
302 shown in Fig. 4. The assumed uncertainty of the synthetic dense WSE significantly affected the calibrated  $M$ ,  
303 which was illustrated by three different cases. With the increase of the uncertainty of UAS altimetry, the weight  
304 of the smoothness term in the objective function increased and the calibrated  $M$  tended to be smoother. When  
305 the uncertainty of UAS altimetry derived WSE increased from 1 cm, to 3 cm and 5 cm, the RMSE of the  
306 calibrated  $M$  changed from 0.7 to 1.06 and 1.93  $\text{m}^{1/3}/\text{s}$  in the high-flow date, i.e., 02/24/2021 (Table 1) and the  
307 RMSE of the calibrated  $M$  increased from 0.39, 1.46 to 2.07  $\text{m}^{1/3}/\text{s}$  in the low-flow date, i.e., 06/02/2020. Some  
308 deviations remained between the calibrated  $M$  and the synthetic  $M$  partly depended on the balance between the  
309 misfit and the smoothness in the objective function, which was determined by trial-and-error.

310 The calibrated  $M$  using partial-coverage WSE showed promising results in the river stretch where  
311 synthetic WSE exists. For detail, the UAS altimetry was concentrated in the chainage of 20 – 30 km and the  
312 calibrated  $M$  agreed well with synthetic truth. Besides, the regularization term of smoothness in the objective  
313 function constrained the spatial variations of the  $M$  in the chainage where UAS altimetry were missing.

314 The calibration was implemented by the global search algorithm, which required tens of thousands of  
315 forward model evaluations, e.g. the total iterations of each simulations in Scenario 1 is 16500, which clearly  
316 illustrated why an efficient forward model is needed.



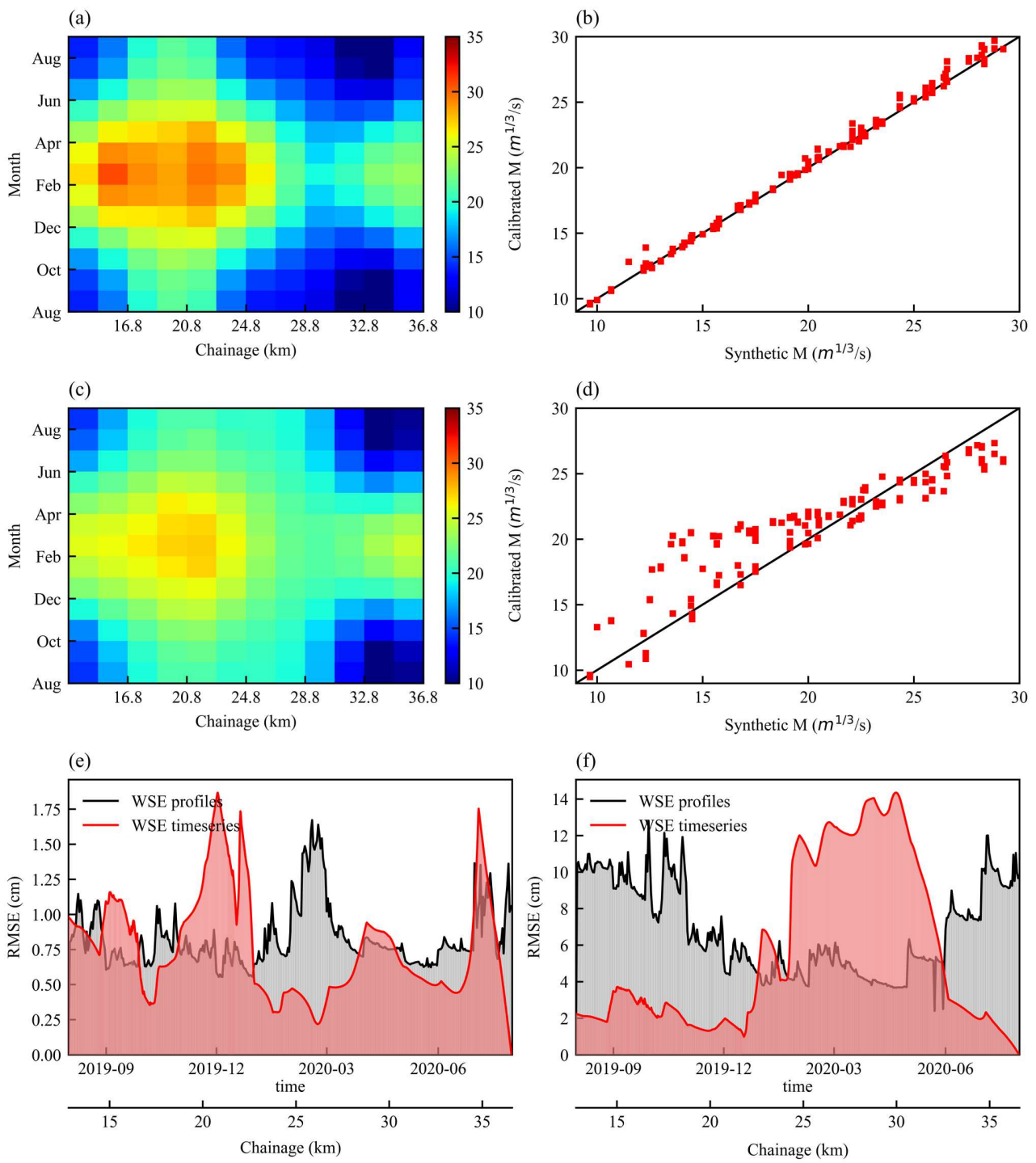
317

318 Figure 4. Calibration results of Manning–Strickler coefficients  $M$  on 02/24/2020 by using synthetic truth of  
 319 WSE fully (a) and partially (b) covered the river stretch. (c) and (d) are the same but for date 06/02/2020. The  
 320 gray areas are river stretch covered by UAS altimetry.

321 Spatiotemporally distributed  $M$  was calibrated by the steady-state solver under the assumptions of  
 322 Scenarios 2 and 3, and the results are displayed in Fig. 5. Generally, the pattern of the  $M$  variation was  
 323 successfully retrieved by the calibration algorithm. The RMSE between the calibrated  $M$  and the synthetic truth  
 324 is  $0.46 \text{ m}^{1/3}/\text{s}$  for Scenario 2 with sufficient WSE. However, the WSE was over fitted by Scenario 2 (Table 1),  
 325 which may indicate that a larger weight for the regularization terms may be appropriate. The RMSE of calibrated  
 326  $M$  is  $2.53 \text{ m}^{1/3}/\text{s}$  for Scenario 3, which is inferior to the calibration results of Scenario 2 due to the limited amount  
 327 of available WSE. The values of  $M$  lower than  $20 \text{ m}^{1/3}/\text{s}$  were significantly overestimated because the available  
 328 WSE observations are insufficient for adequately constraining the parameter.

329 The evaluation results of the simulated WSE against synthetic truth in temporal and spatial scale showed  
 330 that the accuracy of the simulated WSE is high in both time and space under Scenario 2 and Scenario 3. In  
 331 Scenario 2, even though the RMSE shows some spatial (red columns in Fig 5e) and temporal (gray columns in  
 332 the Fig 5f) difference, the overall RMSE is low. The RMSE of the simulated WSE is high in Scenario 3, which  
 333 indicates that the available WSE is insufficient to constrain the variations of  $M$ . The RMSE is high in low-flow  
 334 seasons, e.g., July to December, but the RMSE is low in high-flow seasons, i.e., January to May. Along the

335 chainage, the simulate WSE is less accurate for chainage 20 - 30 km, because M was overestimated compared  
 336 to the synthetic truth in this chainage interval.



337  
 338 Figure 5. Calibration results of Manning–Strickler coefficients  $M$  for Scenario 2 (a, b) and Scenario 3 (c, d). The calibrated  
 339 spatial-temporally varying  $M$  for each scenario is in left columns, and the simulated  $M$  against synthetic truth is in the right  
 340 columns. The accuracy of simulated WSE against synthetic truth displayed in (e) for Scenario 2 and (f) for Scenario 3. The  
 341 red columns represent the accuracy of simulated WSE time series in particular chainage grid. The gray columns represent  
 342 accuracy of simulated longitudinal profile of WSE in each day.

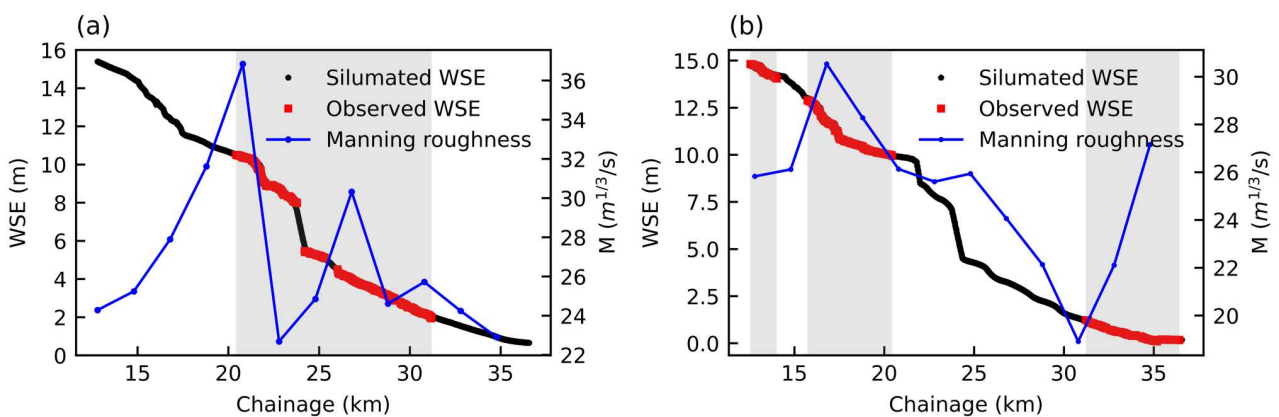
Table 1. Settings for the calibration under different scenarios, together with the efficiency of the calibration algorithms and the calibrated accuracy of WSE, Manning–Strickler coefficients M, three regularization terms and the final objective functions.

Scenario	calibration settings							Efficiency		Accuracy (RMSE)					
	UAS altimetry	Noise (cm)	Weight (w)	Weight ( $\lambda$ )	$\sigma$ (misfit)	$\sigma$ (smoothness)	$\sigma$ (a priori)	Day(s)	Repetitions	WSE (cm)	M ( $m^{1/3}/s$ )	Misfit	Regularization (smoothness)	Regularization (a priori)	Objective function
scenario1	full	1.0	0.09		0.01					2.00	0.70	5029.52	227.95		25.69
	full	3.0	0.05		0.03					3.20	1.06	1424.30	81.73		12.20
	full	5.0	0.02		0.05			1 day		5.67	1.93	1610.09	24.21		7.48
	partial	1.0	0.07	1.0	0.01	0.50		(24/02/2020)	16500	1.97	1.27	2159.79	148.64		17.01
	partial	3.0	0.07		0.03					3.14	1.47	607.41	82.32		10.91
	partial	5.0	0.06		0.05					5.43	1.93	656.83	36.58		8.5907
scenario1	full	1.0	0.02		0.01					1.18	0.39	1746.55	126.90		12.72
	full	3.0	0.02		0.03					3.36	1.46	1570.95	43.44		8.60
	full	5.0	0.02		0.05			1 day		5.19	2.07	1351.27	19.12		6.56
	partial	1.0	0.04	1.0	0.01	0.50		(2/6/2020)	16500	1.12	0.59	744.24	138.00		12.74
	partial	3.0	0.06		0.03					3.12	1.13	638.83	62.72		9.86
	partial	5.0	0.04		0.03					5.51	1.92	717.11	24.68		7.24
Scenario 2	full	3.00	0.07	0.10	0.03	0.50	0.50	12 days	2627010	1.01	0.46	16823.06	2600.39	18.71	37.88
Scenario 3	partial	3.00	0.70	0.10	0.03	0.50	0.50	12 days	2627010	5.38	2.53	5403.77	1406.80	16.70	61.88

## 344 3.2. Real-world calibration for specific dates

345 The synthetic studies demonstrated the ability of the calibration approach to fit spatiotemporally  
 346 distributed Manning–Strickler coefficients  $M$  in general. This section used real-world WSE observations,  
 347 including observations from gauging stations and UAS altimetry, to calibrate  $M$  for Vejle Å. The calibration  
 348 was first implemented for two days, i.e., February 24 and June 02 in 2020, using UAS altimetry, and the results  
 349 are displayed in Fig. 6.  $M$  changed significantly from upstream to downstream on the two different days.  $M$   
 350 declined from  $36 \text{ m}^{1/3}/\text{s}$  to  $24 \text{ m}^{1/3}/\text{s}$  on 02/24/2020 from chainage 20 km to 30 km, and the value decreased from  
 351 30 to  $20 \text{ m}^{1/3}/\text{s}$  on 06/02/2020 in the same area. The landscape shows that dense trees cover the riverbank in this  
 352 river stretch compared to the upstream area where the river flows through farmland and no forests grow along  
 353 the riverbank.

354 The calibration settings and results are displayed in Table 2. The RMSE of the simulated WSE is 8.48  
 355 cm against the UAS altimetry on 02/24/2020 and the value is 6.99 cm on 06/02/2020. The calibrated results are  
 356 not comparable to synthetic study because of the incomplete coverage of UAS altimetry and the structural model  
 357 deficiencies (unsteady-state in reality). The drone surveys were conducted during a day, but the flow conditions  
 358 could have changed especially in high-flow days, e.g., 02/24/2020. Moreover, we merged the UAS altimetry in  
 359 June which we collected in two different dates. Even though we compared the characteristics of the flow regime  
 360 on 06/02/2020 and 06/07/2020 and there are no significant differences, which causes additional model  
 361 uncertainty.



362

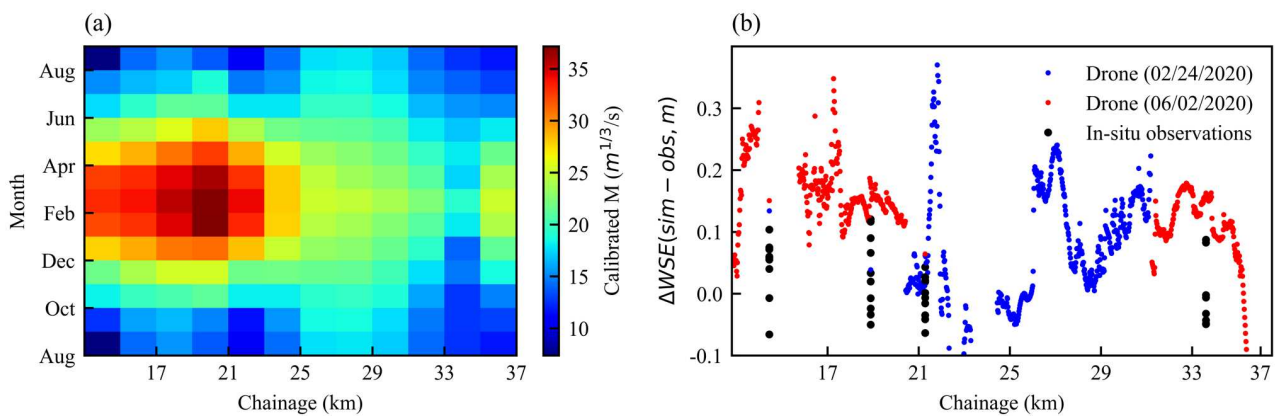
363 Figure 6. Calibration results of Manning–Strickler coefficients  $M$  and the comparison between simulated and UAS  
 364 altimetry derived WSE for two single dates: (a) 2020-Feb and (b) 2020-Jun.

## 365 3.3. Real-world calibration for multiple dates

366 In the real-world calibration of spatial-temporally distributed Manning–Strickler coefficients  $M$ ,  
 367 considering the availability of UAS altimetry data, August 2019 to July 2020 was selected as the calibration

368 period and the validation period was from August 2018 to July 2019, with UAS altimetry data only available in  
369 November and partially covered the river chainage. Steady-state solver and global optimization were used to  
370 search optimal M. Then the calibrated M was used to parameterize the Mike Hydro River model to simulate  
371 continuous time series for each calculation grid.

372 The calibration results of the M and the comparison between simulated and observed WSE are displayed  
373 in Figure 7. The spatio-temporal variation of M is distinctive, high in the cold season (December to April) and  
374 low in the warm season, relatively high upstream of the river and low downstream. In the upstream Vejle Å (12  
375 – 24 km), the bed elevation shows undulating terrain, and the bankfull width and area are changeable in this  
376 area compared to the downstream (Fig.A3). Thus, the complex bathymetry coupled with seasonal growth of  
377 vegetation, resulted in significant changes of M in different seasons in this area. The calibrated M was more  
378 inconsistent in cold season due to the high-flow but relatively stable in warm-season with low-flow. UAS  
379 altimetry and in-situ observations of WSE were used for the steady-state solver calibration, and the RMSE of  
380 the simulated WSE is 7.67 cm (table 2). While a significant bias between simulated WSE and UAS altimetry is  
381 visible, as shown in Fig. 7b. Because a weight between drone data and stations data was used to balance their  
382 corresponding misfit in the objective function. The results indicate that the weight of in-situ data is too large.



383

384 Figure 7. (a) Calibration results of the spatiotemporally distributed Manning–Strickler coefficients  $M$ , and (b)  
385 the difference between simulated WSE and observations along the chainage in Vejle å.

386

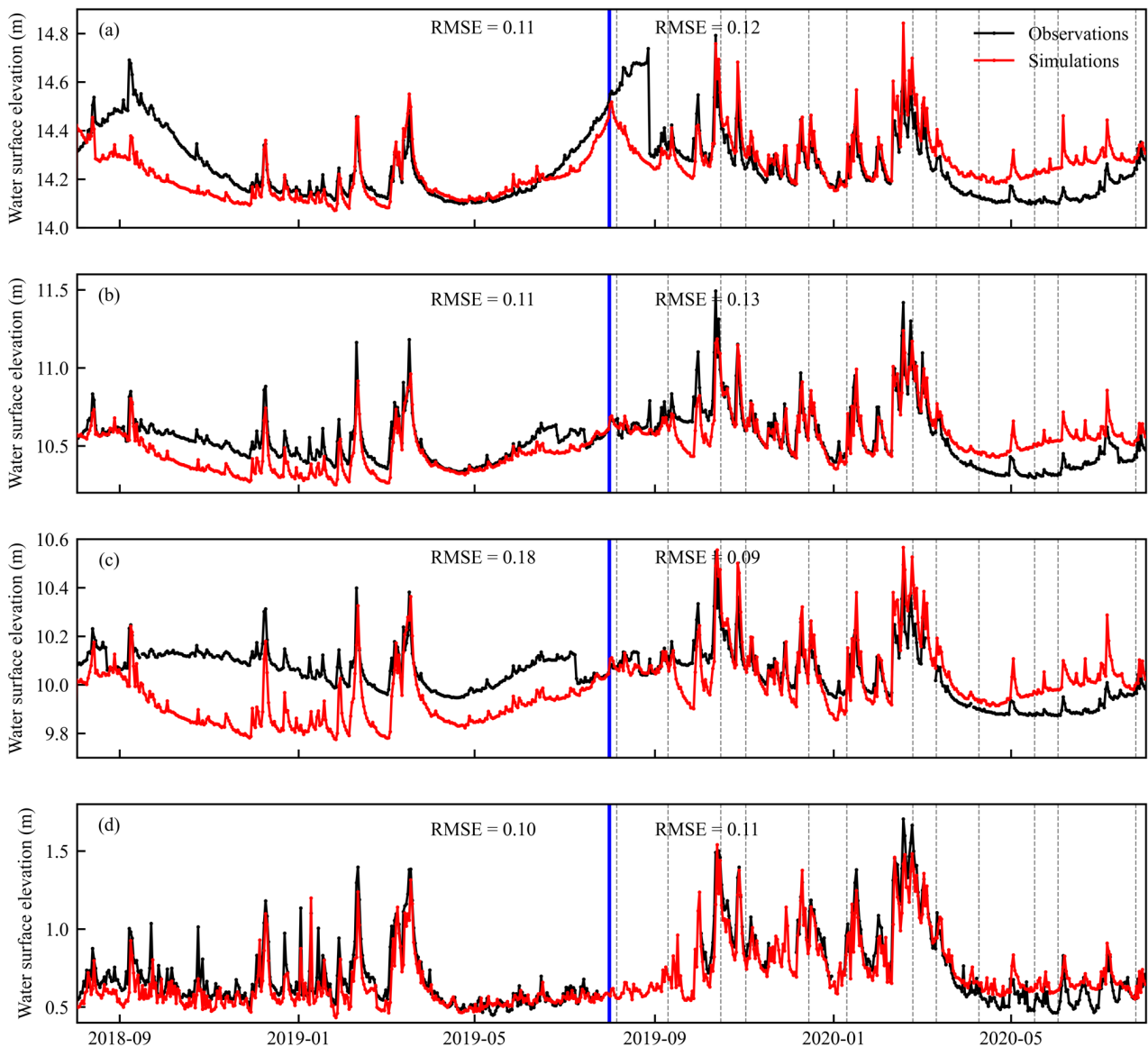
387 Table 2. Settings and results of the calibration with real-world data.

Date (s)	Calibrating settings					Efficiency		Accuracy (RMSE)			Objective function
	Weight (w)	Weight ( $\lambda$ )	$\sigma$ (misfit)	$\sigma$ (smoothness)	$\sigma$ (a priori)	Repetitions	WSE (cm)	Regularization (misfit)	Regularization (smoothness)	Regularization (a priori)	
2/24/2020	0.55	0.00	0.03	0.50	0.50	16500	8.48	5287.50	1288.69	0.00	59.06
6/2/2020							6.99	2943.22	331.93		42.05
12 days	0.07	0.1				2132820	7.67	27689.15	3489.22	311.31	149.26

388

390 The comparison results between the simulated WSE against in-situ observations of four hydrological  
 391 stations are displayed in Figure 8. Generally, the simulated WSE agreed well with in-situ observations in the  
 392 high-flow period, and the simulated WSE is clearly less accurate in the low-flow seasons, which is similar to  
 393 the synthetic study. The overestimation of WSE in low-flow seasons indicated an overestimated of  $M$ .  
 394 Considering the UAS altimetry data we used for calibration in different seasons, the WSE on 02/24/2020 used  
 395 sufficiently for constraining the  $M$ .

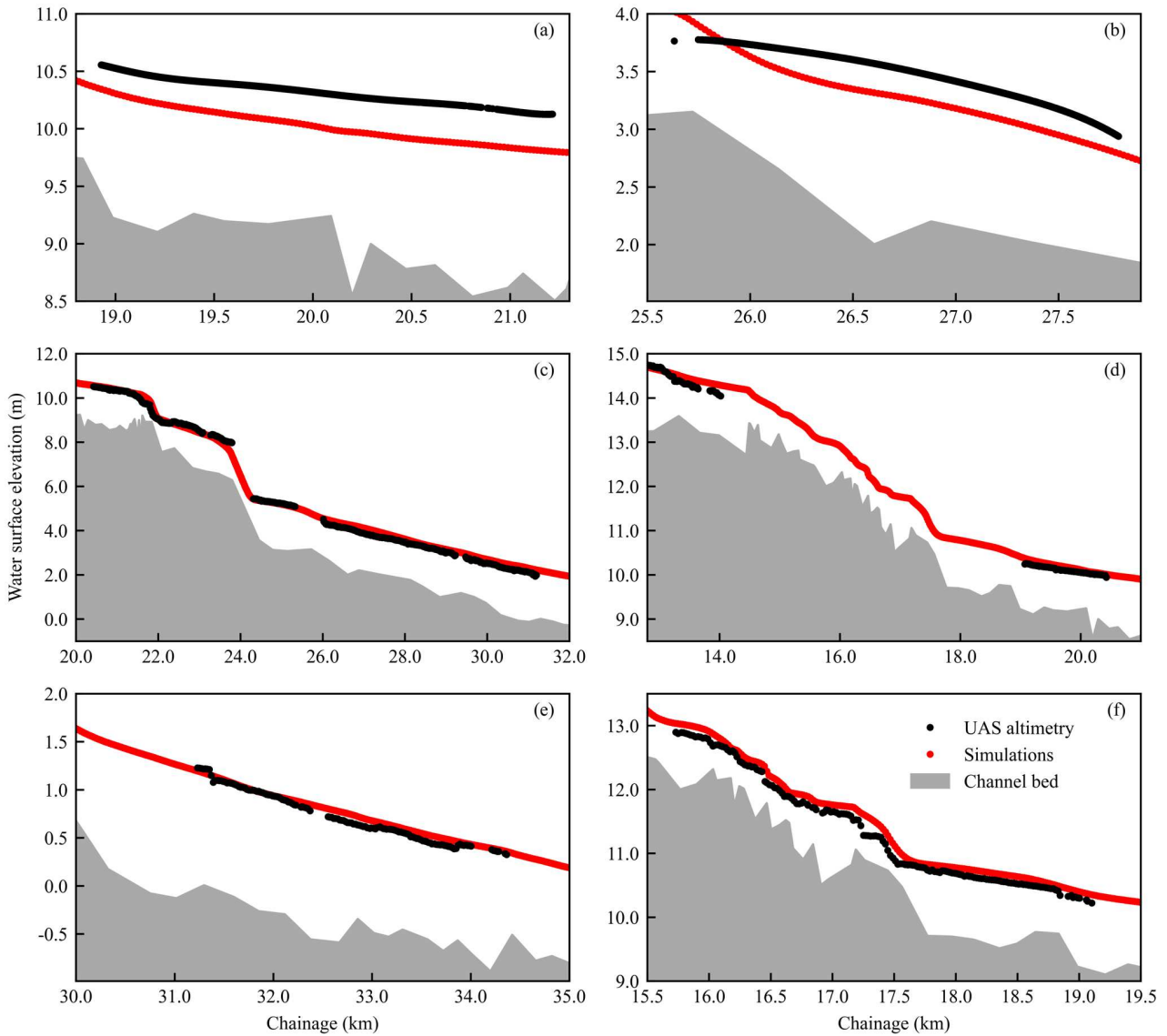
396 Validation results indicated that the calibrated  $M$  were not representative for the validation period,  
 397 especially at Vingsted station (Fig. 8). Spatial patterns and dynamics of vegetation growth may change from  
 398 year to year in which case a longer calibration period is required to obtain more robust parameter estimates.



400 Figure 8. Comparison results of the simulated WSE (by MIKE HYDRO River with steady-state solver calibrated  
401 Manning–Strickler coefficients  $M$ ) against gauging WSE in four hydrological stations: (a) Tørskind, (b)  
402 Raving, (c) Vingsted, and (d) Rosborg. The blue vertical lines divide the simulation period into validation  
403 period (Aug-2018 to Aug-2019) and calibration period. The gray dash vertical lines indicate the WSE was used  
404 for steady-state calibration.

405

406 Figure 9 shows the comparison results of longitudinal profiles of WSE depicted by UAS altimetry and  
407 simulations. The simulated WSE profiles during the validation period, i.e., 11/01/2018 and 11/02/2018, were  
408 underestimated. The simulated WSE is parallel to UAS altimetry observed WSE on 11/1/2018, but the simulated  
409 WSE is underestimated by approximately 0.3 m indicating the estimated  $M$  is too large. The simulated profile  
410 of WSE on 11/02/2018 is lower than observations, and the water surface shows a different slope. The changing  
411 slope in this river stretch is caused by the spatial variation of  $M$  and the bathymetry (Fig. 9b). The simulated  
412 WSE agreed well with the UAS altimetry in the calibration period but was slightly overestimated (Figure 9f).



413

414 Figure 9. Comparison results of simulated WSE against UAS altimetry on: (a) 11/01/2018, (b) 11/02/2018, (c)  
 415 02/24/2020, (d) 06/02/2020 (upstream), (e) 06/02/2020 (downstream), and (f) 06/07/2020.

#### 416 4. Discussion

##### 417 4.1. Impact of density/coverage of WSE observations for calibrating hydraulic models

418 In this study, we used a radar altimetry payload on a UAS to measure the WSE of Vejle Å. The altimetry  
 419 data was smoothed with an interval of 20 m, equivalent to the grid resolution of the steady-state hydraulic solver,  
 420 ensuring that at least one WSE observation fell on each calculation node. The results indicated that the  
 421 parameters were well constrained by dense WSE datasets and the uncertainty had significant effects on the  
 422 calibration results, as illustrated by the synthetic experiments. Potentially, we could further increase the grid  
 423 resolution to 1 m or even less, considering the spatial sampling resolution of WSE by UAS. However,  
 424 calculation efficiency will be decreasing as the number of grid points increased.

425 The advantages of using UAS altimetry data along the chainage were also demonstrated by comparison  
426 to the calibration experiments in which temporally continuous in-situ observations and the MIKE Hydro River  
427 model were used. The calibrated results improved slightly after including UAS altimetry (Fig. B1). Additionally,  
428 UAS altimetry data can be used to calibrate highly resolved Manning–Strickler coefficients  $M$  for a particular  
429 period of interest, for example a flooding period, which was not possible when using in-situ station data only.

430 Additionally, the coverage of the UAS altimetry is essential when spatially variable roughness  
431 parameters are calibrated. As shown by Scenario 1, the calibration results of  $M$  in 06/02/2020 outperformed  
432 02/24/2020. Available UAS altimetry were more continuous in 02/24/2020; even though the spatial variations  
433 of  $M$  were constrained, the fitted roughness coefficient was far away from the truth in the chainage where the  
434 UAS altimetry was missing. In contrast, the available UAS altimetry was more scattered on 06/02/2020.  
435 Although UAS altimetry was missing for short intermittent reaches,  $M$  can be estimated in those reaches thanks  
436 to the smoothness regularization term. However,  $M$  was not well-constrained for longer reaches without  
437 available UAS altimetry data example can be seen in the results for 06/02/2020. We can thus conclude that for  
438 spatio-temporal calibration of the  $M$ , long and continuous UAS altimetry surveys distributed over the seasonal  
439 vegetation growth cycle are critical.

#### 440 4.2. Spatiotemporally varying Manning–Strickler coefficients $M$

441  $M$  is affected by various factors and changes in space and time. The calibrated results in this study  
442 showed that  $M$  of Vejle Å, a stream with high vegetation density, varied from  $10 \text{ m}^{1/3}/\text{s}$  to  $30 \text{ m}^{1/3}/\text{s}$  in both space  
443 and time and changed significantly along the river channel, especially in the human disturbed river segments.  
444 Previous studies have emphasized the spatial variability of  $M$  and pointed out the insufficient representation  
445 achieved with uniform  $M$  for long river reaches (Attari et al., 2021; Attari and Hosseini, 2019; Jiang et al., 2020;  
446 Pappenberger et al., 2007; Werner et al., 2005). Jiang et al.(2020) displayed promising evidence of using  
447 spatially varying  $M$  to predict WSE everywhere along the reach.

448 The growth and cleaning of vegetation and the seasonal variations of discharge affect the variability of  
449  $M$  in time. Vegetation cutting is an important measure to increase cross-sectional conveyance and decrease  
450 floods risks. The  $M$  increased significantly after vegetation cutting, as shown by Jiang et al. (2020). Vegetation  
451 management interventions are not included in the modeling approach presented here, which leads to increased  
452 model uncertainty in the real-world calibration scenarios.

453 The calibration approach for spatial-temporally varying  $M$  can also be used for the rivers with complex  
454 topography and changeable hydraulic conditions. For instance,  $M$  may vary significantly at high stage for  
455 braided and terraced river. Meanwhile, river resistance will be significantly increased by river ice-jams that  
456 cause severe floods in some middle and high latitude rivers, e.g., Yellow River. Thus, a varying  $M$  might  
457 increase the performance of hydrodynamic simulations in such situations.

#### 458 4.3. Potential and limitations of the calibration approach

459 The steady-state solver is efficient and effective for calibrating the  $M$  as shown in the present study. It  
460 took millisecond for the Steady-state solver to simulate WSE in Vejle Å with a resolution of 20 m. Compared  
461 to the hydrodynamic MIKE HYDRO River, the steady-state solver is computationally efficient. To go a step  
462 further, we can use global optimization to fit  $M$  by using this solver. The global optimization is independent of  
463 initial value and capable of avoiding local optima. To calibrate the spatiotemporally distributed  $M$ , the number  
464 of parameters increased significantly. The high resolution of the parameters in space and time increases the  
465 computational requirements for streams or large rivers (Kittel et al., 2021). Moreover, calibration results will  
466 be significantly affected by the chosen regularization strategy.

467 The present calibration algorithm for spatio-temporally distributed  $M$  has several drawbacks. In the  
468 hydraulic model, we used the cross-sectional information to delineate the river channel, and the cross-sections  
469 were linearly interpolated for each calculation node from the limited in-situ data. Thus, the accuracy,  
470 representation and density of the surveyed bathymetry is critical for the calculation. The 1-D steady-state  
471 hydraulic solver is based on the Saint-Venant equation, and it is insufficient to simulate overbank water flow.  
472 For such situations, a 1D-2D hydraulic model would be required. That is a reason for the relatively high error  
473 of the simulated water level in February in Vejle Å. For the regularization term, we assumed that  $M$  of natural  
474 rivers was characterized by spatial continuity and changes smoothly. However, most of the natural rivers have  
475 been affected by human activities, for example, the construction of reservoirs and dams, vegetation management,  
476 etc., which will often result in abrupt changes of hydraulic properties. Additionally, we introduced different  
477 weights for regularization terms which are determined by trial-and-error method. A more comprehensive  
478 method to select optimal weights for the regularization terms is the L-curve approach, which aims to  
479 compromise data misfit and the regularization terms (Hansen and O’Leary, 1993). However, implementation of  
480 such methods requires a large amount of computational resources.

## 481 **5. Conclusion**

482 This study presented a calibration approach for spatiotemporally distributed Manning–Strickler  
483 coefficients  $M$  by combining UAS altimetry and in-situ stations. Several synthetic experiments under different  
484 assumptions were evaluated and used to demonstrate the feasibility and efficiency of the scheme. We then  
485 applied the approach in a real-world case study, an approximately 20 km river stretch of Vejle Å, to calibrate  
486 and validate the  $M$ .

487 The synthetic study shows that  $M$  could be well-calibrated by the dense sampling of WSE in both spatial  
488 and temporal scale. The synthetic calibration experiments showed that standard errors of ca. 3 cm on the WSE,  
489 as achieved with our current UAS radar altimetry system, are sufficient to constrain spatio-temporal variations  
490 of hydraulic roughness. Meanwhile, the steady-state solver is efficient and effective in simulating the WSE  
491 along the river course, which is a requirement for the implementation of global search algorithms for highly  
492 parameterized inverse problems.

493 The calibration algorithm was further applied on a real-world dataset to fit the optimal sets of M with  
494 limited gauging data and UAS altimetry. The calibration results indicated that the M of Vejle Å changed  
495 significantly in space and time. The simulated WSE has a RMSE of 8.48 cm on a high-flow day and 6.99 cm  
496 on a low-flow day compared to highly resolved UAS altimetry. The simulated time series of WSE at four  
497 hydrological stations have an average RMSE of 10 cm after we transferred the M calibrated by the steady-state  
498 solver to the hydrodynamic model.

499

#### 500 **Acknowledgements:**

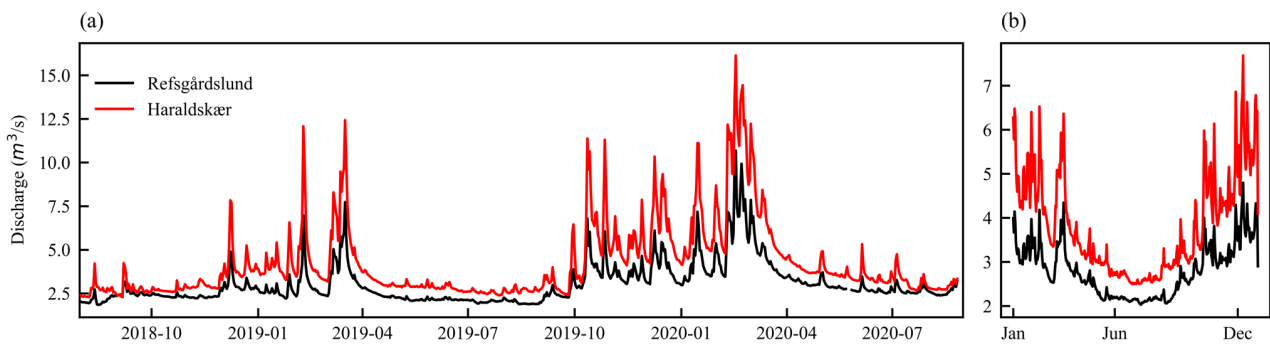
501 This study was supported by Innovation Fund Denmark through the projects Riverscapes (file number 7048-  
502 00001B) and ChinaWaterSense (file number: 8087-00002B) and by the National Key Research and  
503 Development Program of China project (2018YFE0106500). The first author was supported by a scholarship  
504 from the China Scholarship Council (CSC).

505

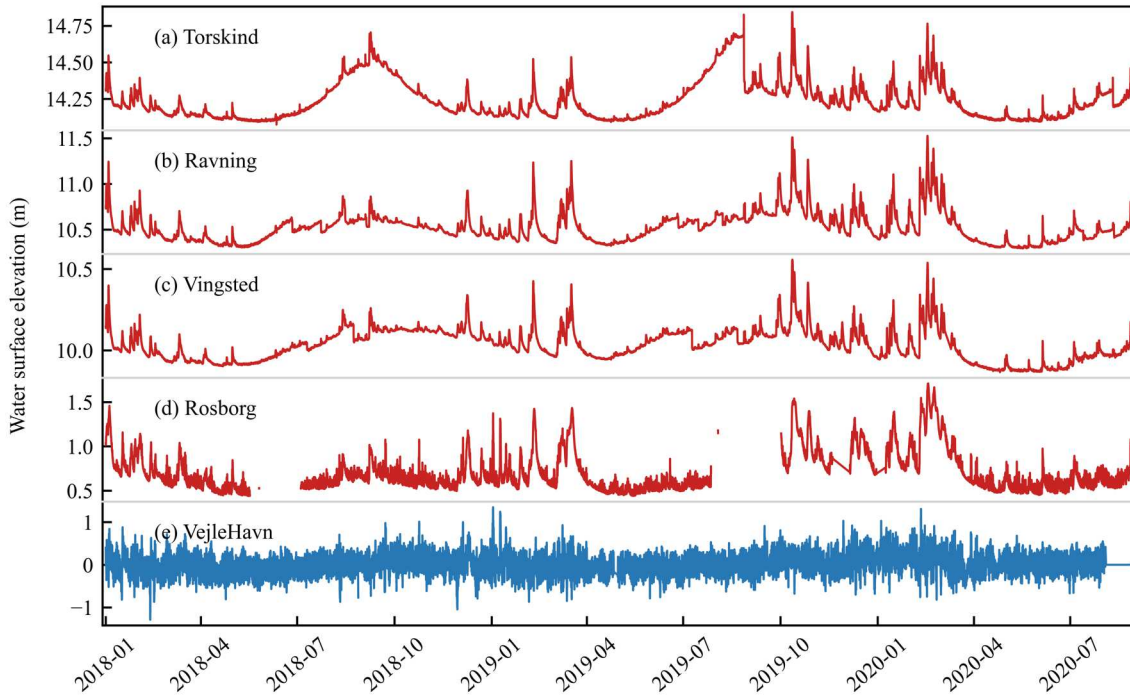
#### 506 **Appendix**

507 **Appendix A.** In-situ observations of discharge, water surface elevation and bathymetric information in Vejle  
508 Å.

509

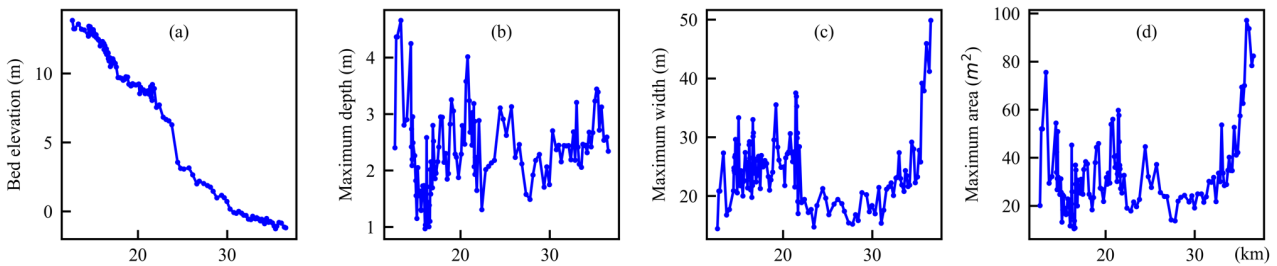


510 [Figure A1.](#) Discharge monitored by two hydrological stations (Refsgårdslund and Haraldskær) in the period of Jan 2018  
511 [to Aug 2020.](#)



512

513 Figure A2. Water surface elevation monitored by five hydrological stations (Tørskind, Ravning, Vingsted, Rosborg, Vejle  
 514 Haven) in the period of Jan 2018 to Aug 2020.



515

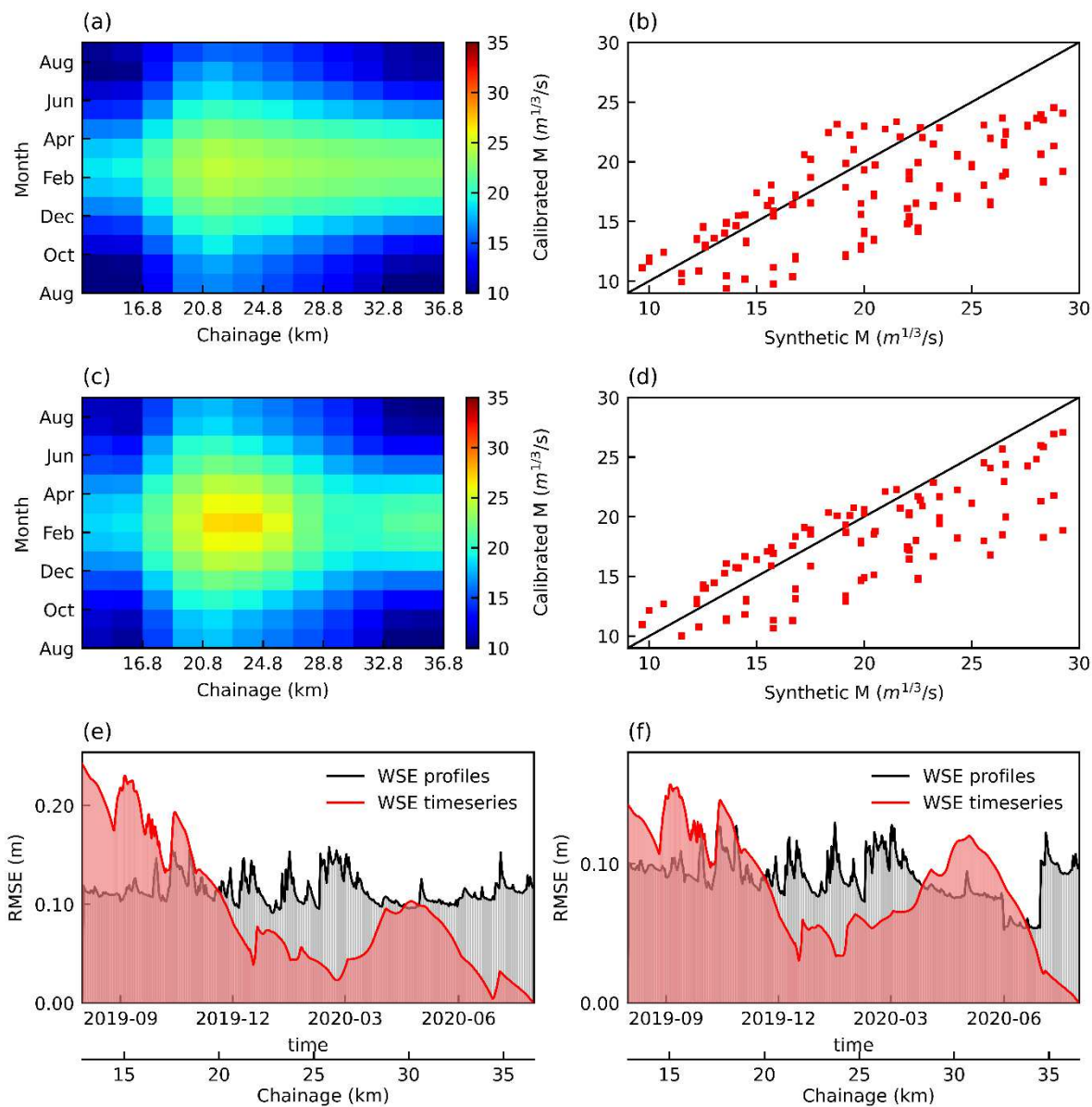
516 Figure A3. Basic information of the 130 cross sections, including (a) bed elevation, (b) bank full depth, (c) bank full width  
 517 and (d) bank full area.

518 **Appendix B.** Synthetic experiment for the calibration of MIKE Hydro River model by using Levenberg-Marquardt local  
 519 optimization method.

520 Scenario B1: Calibration of spatiotemporally varying Manning–Strickler coefficients  $M$  using in-situ  
 521 data only. This scenario is set for a river stretch monitored by discretely distributed monitoring stations.  
 522 Considering that the station data was continuously collected with a short time interval, lots of information will  
 523 be lost if we utilize only a few days for steady-state calibration. Here, the MIKE Hydro River model is used for  
 524 WSE simulating, and the local optimization is used for calibrating  $M$ . The initial value is essential for the  
 525 optimization, and the initial  $M$  was set to  $20 \text{ m}^{1/3}/\text{s}$  for all the river stretches. Please be aware that it is extremely

526 time-consuming if we set the calculation grid spacing as 20 m when using the MIKE Hydro River model for  
527 Vejle case, thus propagations only calculated in each cross section.

528 Scenario B2: this scenario is the same as the former one, but with additional UAS altimetry collected  
529 in February and June 2020 and partially covered Vejle Å, as shown in Figure 6b.



530

531 Figure B1. Calibration results of synthetic experiment for Scenario C1 and C2 for calibrating MIKE HYDRO River model  
532 by using local optimization method: (a) the calibrated spatiotemporally distributed Manning–Strickler coefficients  $M$ , and  
533 (b) 1-1 line between the calibrated  $M$  and the synthetic truth for Scenario B1; (c) and (d) are the same but for Scenario B2;  
534 the accuracy of the simulated WSE are displayed in (e) for Scenario B1 and (d) for Scenario B2.

535 **References**

- 536 Attari, M., Hosseini, S.M., 2019. A simple innovative method for calibration of Manning's roughness  
537 coefficient in rivers using a similarity concept. *J. Hydrol.* 575, 810–823.  
538 <https://doi.org/10.1016/j.jhydrol.2019.05.083>
- 539 Attari, M., Taherian, M., Hosseini, S.M., Niazmand, S.B., Jeiroodi, M., Mohammadian, A., 2021. A simple  
540 and robust method for identifying the distribution functions of Manning's roughness coefficient along a  
541 natural river. *J. Hydrol.* 595, 125680. <https://doi.org/10.1016/j.jhydrol.2020.125680>
- 542 Bandini, F., Jakobsen, J., Olesen, D., Reyna-Gutierrez, J.A., Bauer-Gottwein, P., 2017. Measuring water level  
543 in rivers and lakes from lightweight Unmanned Aerial Vehicles. *J. Hydrol.* 548, 237–250.  
544 <https://doi.org/10.1016/J.JHYDROL.2017.02.038>
- 545 Bandini, F., Sunding, T.P., Linde, J., Smith, O., Jensen, I.K., Köppl, C.J., Butts, M., Bauer-Gottwein, P.,  
546 2020. Unmanned Aerial System (UAS) observations of water surface elevation in a small stream:  
547 Comparison of radar altimetry, LIDAR and photogrammetry techniques. *Remote Sens. Environ.*  
548 <https://doi.org/10.1016/j.rse.2019.111487>
- 549 Blöschl, G., Kiss, A., Viglione, A., Barriendos, M., Böhm, O., Brázdil, R., Coeur, D., Demarée, G., Llasat,  
550 M.C., Macdonald, N., Retsö, D., Roald, L., Schmocker-Fackel, P., Amorim, I., Bělinová, M., Benito, G.,  
551 Bertolin, C., Camuffo, D., Cornel, D., Doktor, R., Elleder, L., Enzi, S., Garcia, J.C., Glaser, R., Hall, J.,  
552 Haslinger, K., Hofstätter, M., Komma, J., Limanówka, D., Lun, D., Panin, A., Parajka, J., Petrić, H.,  
553 Rodrigo, F.S., Rohr, C., Schönbein, J., Schulte, L., Silva, L.P., Toonen, W.H.J., Valent, P., Waser, J.,  
554 Wetter, O., 2020. Current European flood-rich period exceptional compared with past 500 years. *Nature*  
555 583, 560–566. <https://doi.org/10.1038/s41586-020-2478-3>
- 556 Cowan, W.L., 1956. Estimating hydraulic roughness coefficients. *Agric. Eng.* 37, 473–475.
- 557 Duan, Q., Sorooshian, S., Gupta, V., 1992. Effective and efficient global optimization for conceptual rainfall-  
558 runoff models. *Water Resour. Res.* 28, 1015–1031.
- 559 Duan, Q.Y., Gupta, V.K., Sorooshian, S., 1993. Shuffled complex evolution approach for effective and  
560 efficient global minimization. *J. Optim. Theory Appl.* 76, 501–521.
- 561 Hansen, P.C., O'Leary, D.P., 1993. The use of the L-curve in the regularization of discrete ill-posed problems.  
562 *SIAM J. Sci. Comput.* 14, 1487–1503.
- 563 Henkel, T., Wilson, H., Krug, W., 2012. Global sensitivity analysis of nonlinear mathematical models - An  
564 implementation of two complementing variance-based algorithms. *Proc. - Winter Simul. Conf.*  
565 <https://doi.org/10.1109/WSC.2012.6465065>
- 566 Houska, T., Kraft, P., Chamorro-Chavez, A., Breuer, L., 2015. SPOTting model parameters using a ready-  
567 made python package. *PLoS One* 10, e0145180.

- 568 Hunter, N.M., Bates, P.D., Horritt, M.S., Wilson, M.D., 2007. Simple spatially-distributed models for  
569 predicting flood inundation: A review. *Geomorphology* 90, 208–225.  
570 <https://doi.org/10.1016/j.geomorph.2006.10.021>
- 571 Jiang, L., Bandini, F., Smith, O., Klint Jensen, I., Bauer-Gottwein, P., 2020. The Value of Distributed High-  
572 Resolution UAV-Borne Observations of Water Surface Elevation for River Management and  
573 Hydrodynamic Modeling. *Remote Sens.* 12, 1171. <https://doi.org/10.3390/rs12071171>
- 574 Jiang, L., Madsen, H., Bauer-Gottwein, P., 2019. Simultaneous calibration of multiple hydrodynamic model  
575 parameters using satellite altimetry observations of water surface elevation in the Songhua River.  
576 *Remote Sens. Environ.* 225, 229–247. <https://doi.org/10.1016/J.RSE.2019.03.014>
- 577 Kittel, C.M.M., Hatchard, S., Neal, J.C., Nielsen, K., Bates, P.D., Bauer-Gottwein, P., 2021. Hydraulic model  
578 calibration using CryoSat-2 observations in the Zambezi catchment. *Water Resour. Res.* 1–19.  
579 <https://doi.org/10.1029/2020wr029261>
- 580 Knox, J.C., 1993. Large increases in flood magnitude in response to modest changes in climate. *Nature* 361,  
581 430–432. <https://doi.org/10.1038/361430a0>
- 582 Lee, J., Perera, D., Glickman, T., Taing, L., 2020. Water-related disasters and their health impacts: A global  
583 review. *Prog. Disaster Sci.* 8, 100123. <https://doi.org/10.1016/j.pdisas.2020.100123>
- 584 Li, S.-G., Venkataraman, L., McLaughlin, D., 1992. Stochastic theory for irregular stream modeling. Part I:  
585 flow resistance. *J. Hydraul. Eng.* 118, 1079–1090.
- 586 Marjoribanks, T.I., Hardy, R.J., Lane, S.N., 2014. The hydraulic description of vegetated river channels: the  
587 weaknesses of existing formulations and emerging alternatives. *Wiley Interdiscip. Rev. Water* 1, 549–  
588 560. <https://doi.org/10.1002/wat2.1044>
- 589 Mtamba, J., van der Velde, R., Ndomba, P., Zoltán, V., Mtaló, F., 2015. Use of Radarsat-2 and Landsat TM  
590 Images for Spatial Parameterization of Manning’s Roughness Coefficient in Hydraulic Modeling.  
591 *Remote Sens.* 7, 836–864. <https://doi.org/10.3390/rs70100836>
- 592 Pappenberger, F., Beven, K., Frodsham, K., Romanowicz, R., Matgen, P., 2007. Grasping the unavoidable  
593 subjectivity in calibration of flood inundation models: A vulnerability weighted approach. *J. Hydrol.*  
594 333, 275–287. <https://doi.org/10.1016/j.jhydrol.2006.08.017>
- 595 Rokaya, P., Morales-Marin, L., Lindenschmidt, K.E., 2020. A physically-based modelling framework for  
596 operational forecasting of river ice breakup. *Adv. Water Resour.* 139, 103554.  
597 <https://doi.org/10.1016/j.advwatres.2020.103554>
- 598 Sauer, I.J., Reese, R., Otto, C., Geiger, T., Willner, S.N., Guillod, B.P., Bresch, D.N., Frieler, K., 2021.  
599 Climate signals in river flood damages emerge under sound regional disaggregation. *Nat. Commun.* 12,

600 1–11. <https://doi.org/10.1038/s41467-021-22153-9>

601 Shi, H., Li, T., Liu, R., Chen, J., Li, J., Zhang, A., Wang, G., 2015. A service-oriented architecture for  
602 ensemble flood forecast from numerical weather prediction. *J. Hydrol.* 527, 933–942.  
603 <https://doi.org/10.1016/j.jhydrol.2015.05.056>

604 Tuozzolo, S., Langhorst, T., de Moraes Frasson, R.P., Pavelsky, T., Durand, M., Schobelock, J.J., 2019. The  
605 impact of reach averaging Manning’s equation for an in-situ dataset of water surface elevation, width,  
606 and slope. *J. Hydrol.* 578. <https://doi.org/10.1016/j.jhydrol.2019.06.038>

607 Vélez-Nicolás, M., García-López, S., Barbero, L., Ruiz-Ortiz, V., Sánchez-Bellón, Á., 2021. Applications of  
608 Unmanned Aerial Systems (UASs) in Hydrology: A Review. *Remote Sens.* 13, 1359.  
609 <https://doi.org/10.3390/rs13071359>

610 Werner, M.G.F., Hunter, N.M., Bates, P.D., 2005. Identifiability of distributed floodplain roughness values in  
611 flood extent estimation. *J. Hydrol.* 314, 139–157. <https://doi.org/10.1016/j.jhydrol.2005.03.012>

612 Ye, A., Zhou, Z., You, J., Ma, F., Duan, Q., 2018. Dynamic Manning’s roughness coefficients for  
613 hydrological modelling in basins. *Hydrol. Res.* 49, 1379–1395. <https://doi.org/10.2166/nh.2018.175>

614